



Non-resonant phase sensitive approach for time resolved microwave conductivity in photoactive thin films

Jasleen K. Bindra^{a,b}, Pragya R. Shrestha^{a,c}, Sebastian Engmann^{a,c}, Chad D. Cruz^a, David J. Gundlach^a, Emily G. Bittle^a, Jason P. Campbell^{a,*}

^a Nanoscale Device Characterization Division, National Institute of Standards and Technology, Gaithersburg, MD, USA

^b Institute for Research in Electronics and Applied Physics, University of Maryland, MD, USA

^c Theiss Research, La Jolla, CA, USA

ARTICLE INFO

Keywords:

Time resolved microwave conductivity
Transient photoconductivity
Organic semiconductors
Phase sensitive detection

ABSTRACT

Time-resolved microwave conductivity (TRMC) is a contactless technique utilized for the investigation of carrier density, transport properties, trapping phenomena, and recombination parameters in charge transport materials. Traditional TRMC methods rely on resonant cavities or resonators, which impose limitations on the frequency range and accuracy of measurements. In this study, we introduce an innovative approach that employs a non-resonant coplanar transmission line and a microwave interferometric detection scheme to investigate the phase-dependent complex microwave conductivity. Additionally, we demonstrate unique calibration techniques for determining the absolute complex microwave conductivity by combining transient photoconductivity (TPC) and electron spin resonance (ESR) as complementary methods. By utilizing a phase-sensitive microwave interferometer, our detection scheme significantly enhances measurement sensitivity and eliminates the need for a resonant cavity. This broadband detection system enables direct measurement of phase-dependent changes in film conductivity ($\Delta\sigma$). Moreover, it allows us to measure subtle variations in sample photoconductivity upon optical excitation and accommodates greatly restricted volumes (\sim nL) consistent with typical device sizes. Here we demonstrate the utility of this technique on a series of poly(3-hexylthiophene) (P3HT) and the electron acceptor [6,6]-phenylC61-butyric acid methyl ester (PCBM) thin films with varying concentrations of PCBM and film thickness.

1. Introduction

Time-resolved microwave photoconductivity (TRMC) is a technique that allows for qualitative and quantitative measures of light-induced changes in bulk film conductivity [1–6]. These conductivity changes can be related to charge generation, separation, and recombination by measurement of the changes in bulk microwave impedance [7–10]. Understanding the dynamics of charge carriers in semiconductors holds significant importance in comprehending the electronic and material properties of a system. Moreover, it plays a vital role in the design and optimization of devices. This significance is particularly critical when it comes to organic semiconductor-based solar cells, light-emitting diodes, and transistors. In these devices, the processes of charge generation, extraction, and amplification rely heavily on the dynamic behavior of the photogenerated carriers. In contrast to most other photo-induced charge dynamics measurements [11–20], TRMC is a contactless

technique that avoids the necessity to apply ohmic contacts and therefore eliminates effects due to active layer-contact interfaces [7–10]. However, conventional TRMC which uses a microwave resonant cavity is restricted in application due to the large volume of sample required along with the need to match measurement frequency to that of the cavity. We therefore present a novel measurement using a broadband co-planar transmission line which allows for phase-dependent conductivity measurements of small area thin films in similar geometries and volumes as standard electronic and opto-electronic devices.

TRMC measurements can be performed on a range of samples, including crystals, thin films, powders, or discontinuous films [21–25]. Its utility has been employed to study the transfer, transport, recombination, and trapping of photogenerated charges in novel materials such as organic semiconductors, quantum dots, chalcogenides, dye-sensitized scaffolds, metal oxides, carbon nanotubes, and perovskites [25–30]. At its core, TRMC can be understood as a pump–probe technique in which

* Corresponding author.

E-mail address: jason.campbell@nist.gov (J.P. Campbell).

<https://doi.org/10.1016/j.mtadv.2024.100471>

Received 10 November 2023; Received in revised form 22 January 2024; Accepted 27 January 2024

Available online 7 February 2024

2590-0498/Published by Elsevier Ltd. This is an open access article under the CC BY-NC-ND license (<http://creativecommons.org/licenses/by-nc-nd/4.0/>).

illumination by a nanosecond pulsed laser at energies above the band gap serves as a pump and microwaves (GHz) are used as a probe to measure the resulting change in impedance/conductance of a photoactive material. The conventional TRMC setup consists of the following essential parts: (1) a stable microwave source usually at X-band, (2) a photo-excitation source, (3) a microwave cell/resonant cavity loaded with the sample of interest, and (4) a sensitive detection and data acquisition system. The sample cell consists either of a simple shorted waveguide section, a specially designed waveguide/microwave cavity [1–4], or a planar resonator [31]. Typically, the samples are placed in the resonant cavity at a position of maximum microwave electric field and the photoexcitation occurs through a grating in the resonant cavity [32]. The photo-induced change in total sample volume conductivity alters the overall impedance which is sensed as a change in the reflected microwave power. The sample positioning and cavity tuning can introduce large experimental uncertainties which impact overall sensitivity and repeatability [33].

This study presents an approach for investigating the complex microwave conductivity of volume limited organic and inorganic semiconducting thin films (Fig. 1a and b). It utilizes a phase-sensitive detection scheme, and the simplicity of the experimental setup allows for compatibility with other in-operando techniques such as Electron Spin Resonance (ESR) and Time-Resolved Photocurrent (TPC). The versatility of this approach, particularly in measuring volume-limited samples, has the potential to pave the way for new discoveries and a deeper understanding of the physics underlying the recent reports of

magneto-optical effects in organic semiconductors [34]. A combination of non-resonant sample-microwave coupling, and interferometric microwave detection leads to a highly sensitive and accessible experimental setup, see Fig. 1a and b. The sensitivity gains achieved by opting for an interferometric detection scheme, as opposed to a conventional resonant scheme, enable investigations of remarkably small regions of the semiconducting films, with dimensions on the order of device sizes (mm^2/nL), as illustrated in Fig. S2. These dimensions establish a direct correlation to fully processed devices. Fig. 1c shows a representative kinetic trace of P3HT:PCBM blend film (1:1 in vol % fraction) at 9 GHz microwave frequency and $10 \mu\text{J}/\text{cm}^2$ laser fluence in ambient conditions. An average of 10–1000 transients (10 Hz repetition rate) yields signal to noise ratio of >150 . Moreover, the measurement allows for unambiguous resolution of the complex photoconductivity components verified by a companion ESR measurement.

The key photoexcitation and microwave detection innovations utilized in this study are related to interferometric detection methods detailed in recent reports [35,36]. The TRMC system used in this study consists of the following parts as illustrated in Figs. 1a and 2: (a) a stable microwave source, (b) microwave excitation and detection circuitry, (c) co-planar transmission line with the sample of interest (d) a nanosecond pulsed laser, and (e) an electromagnet with modulation coils. The electromagnet with modulation coils included in this setup is used for companion ESR measurements to resolve the complex photoconductivity.

The microwave detection circuitry couples to the photoactive sample

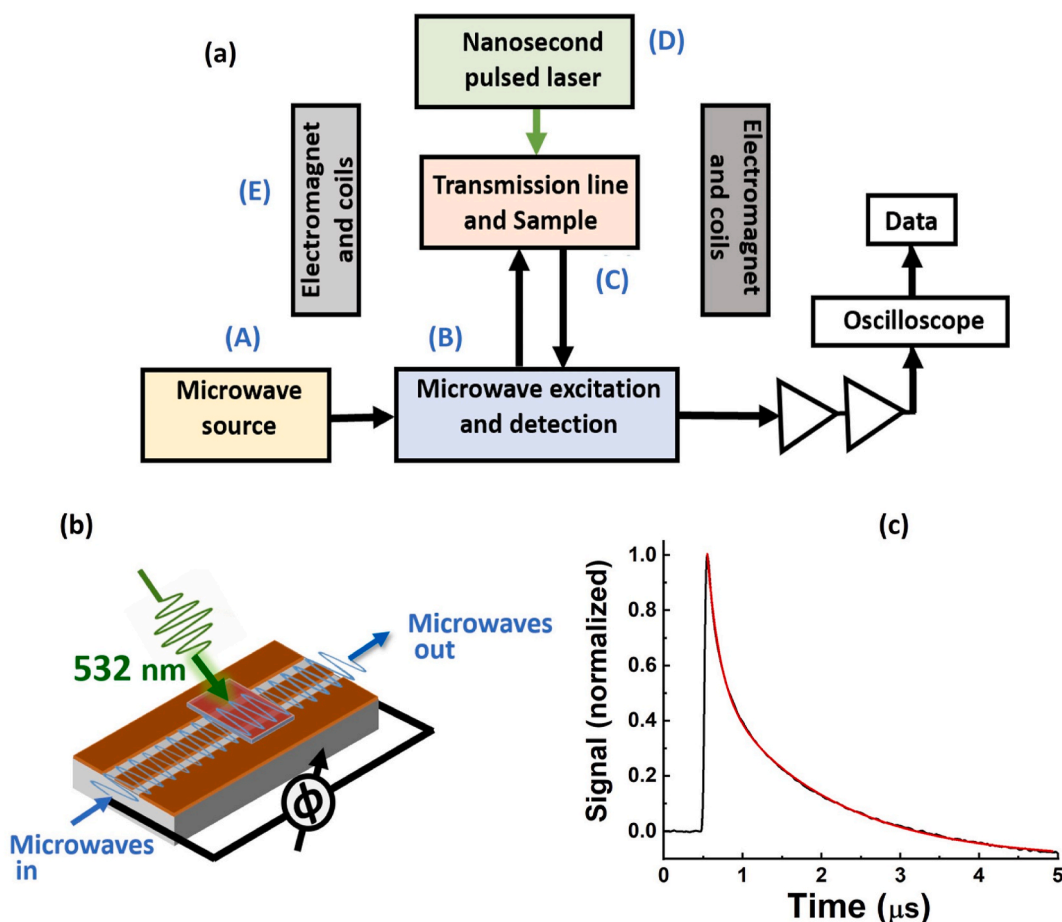


Fig. 1. (a) Illustration of TRMC setup with (A) microwave source, (B) sample uniformly illuminated by laser (spot size $\sim \text{cm}^2$), microwave excitation and detection circuitry, (C) sample assembly, (D) nanosecond pulsed laser and (E) an electromagnet with modulation coils. (b) Schematic of a co-planar transmission line with thin films of photoactive materials on glass. (c) Experiment (black) TRMC kinetic trace of P3HT:PCBM blend film (1:1 in wt % fraction) at 9 GHz microwave frequency and $10 \mu\text{J}/\text{cm}^2$ laser fluence in ambient conditions and its fit to a biexponential function (red). (For interpretation of the references to color in this figure legend, the reader is referred to the Web version of this article.)

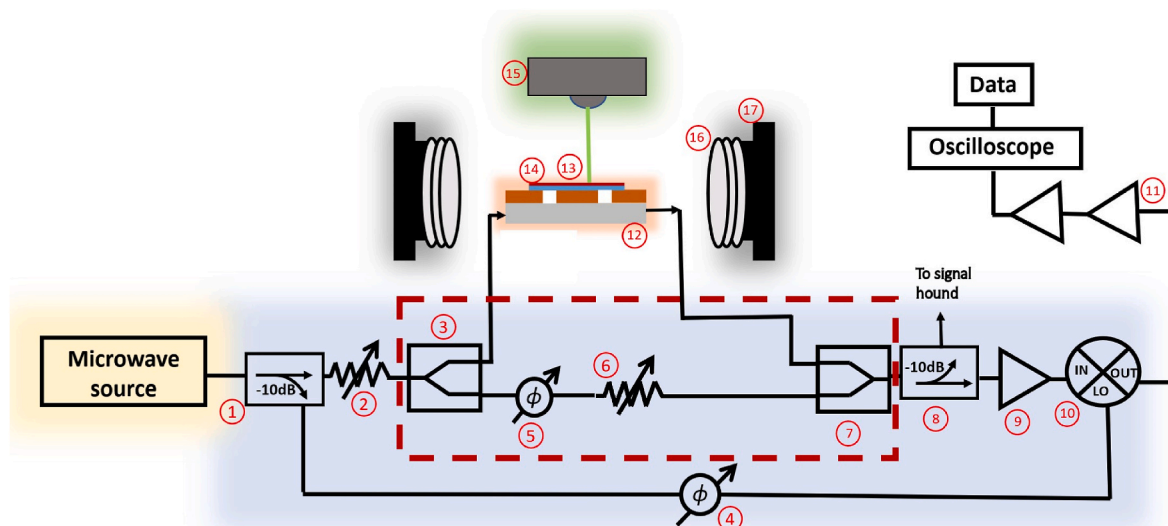


Fig. 2. Detailed schematic of TMRC setup with microwave source, (1)–(11) are the parts of the microwave bridge including microwave excitation and detection circuitry: 10 dB couplers (1) and (8), variable attenuators (2) and (6), splitter (3), phase-shifters (4) and (5), combiner (7), rf amplifier (9), mixer (10) and low noise amplifier (11). (15) is the nanosecond pulsed laser (16) and (17) are an electromagnet with modulation coils used for companion ESR measurements. The background color scheme represents the same components from those in Fig. 1a and hereafter will represent the same in the following figures. (For interpretation of the references to color in this figure legend, the reader is referred to the Web version of this article.)

using a non-resonant co-planar transmission line, Figs. 2 and 3. The transmission line is the conduit to couple both the microwave electric (E_1) and microwave magnetic (B_1) fields into the photoactive films which are deposited on glass. These films were secured on the transmission line with sample facing the transmission line (Fig. 3a and b). A finite element-based transmission line parameter calculator was used to optimize the transmission line parameters to achieve an impedance of $\sim 50 \Omega$ with a maximum E_1 field strength (Fig. 3c and d). A cross-sectional schematic of the co-planar transmission line (no bottom ground plane) is shown in Fig. 3b. Here w is the width of the central track, g is the gap width, t is the thickness of the copper film and h is the substrate dielectric thickness. For the non-resonant transmission line design, the magnitude of the E_1 field is determined by (1) the thickness of the dielectric, and (2) the amplitude of the high-frequency input voltage signal. Reducing the dielectric thickness can increase the magnitude of E_1 , but it also effectively limits the sample volume due to

its relationship with the signal line width, w (smaller h requires a small w for the same impedance) [37]. To further maximize the E_1 strength, the bottom ground plane was removed. This concentrates the E-field above the substrate rather than within the substrate.

The sample assembly (Fig. 3a) was connected to the sample arm of the microwave interferometer using SMA connectors and coax cables. A stable microwave source provides microwave frequencies in the range 8.5 GHz–10.5 GHz. The microwave detector employed in this study is discussed in detail elsewhere [35] but briefly described here for completeness. A 10 dB coupler was used to split the input microwaves into a reference signal for an X-band mixer’s local oscillator input and an input to the interferometer (Fig. 2). The interferometer is configured in a Mach-Zehnder geometry (Fig. 2 red-dashed box) in which a reference signal is tuned to destructively interfere with a signal that interacts with the sample in the absence of optical excitation. In this configuration, the interferometer together with the low noise amplifier and a x-band mixer

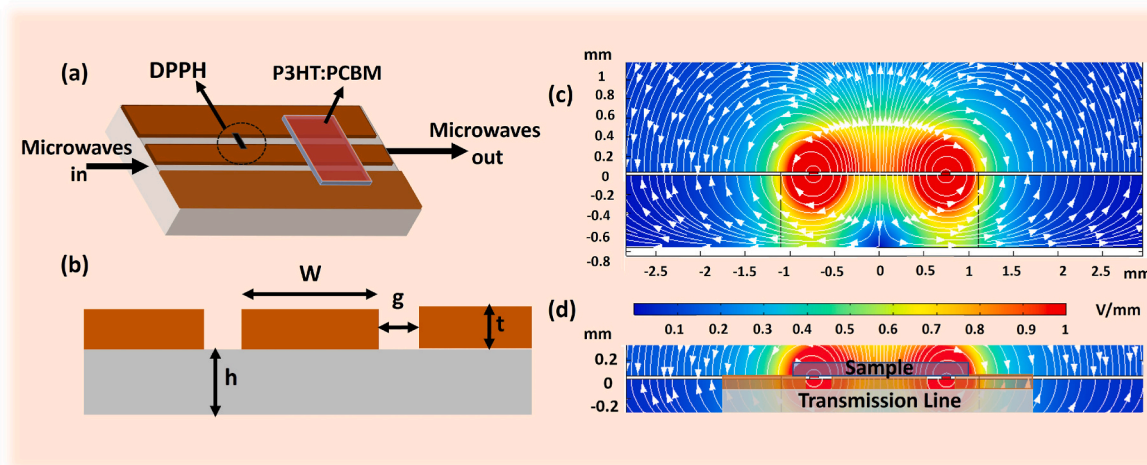


Fig. 3. (a) Sample assembly on a non-grounded co-planar transmission line with a photoactive thin film on a glass substrate and a DPPH-infused paper strip for phase-sensitive (ESR) measurements. (b) Schematic of a cross-section of the co-planar transmission line without backplane. (c) Finite element simulation for a $\approx 50 \Omega$ non-grounded co-planar transmission line with $w = 1.38 \text{ mm}$, $g = 0.15 \text{ mm}$, $t = 35 \mu\text{m}$ and $h = 0.76 \text{ mm}$. (d) Cross-section of transmission line overlaid with finite element simulation demonstrating the placement of sample at the E_1 maximum.

provides the detection sensitivity that can exceed the sensitivity achieved with typical resonant cavity detection methods. Upon careful tuning of the interferometer, the detection sensitivity can far exceed that achieved with typical resonant cavity detection methods [35]. Pulsed photoexcitation alters the conductivity of the sample and consequent impedance of the transmission line/sample system. The output of the microwave interferometer is amplified before demodulation using an X-band mixer. The demodulated transient signal is further amplified by a series of low-noise amplifiers and collected using a high-resolution digital oscilloscope.

The sample excitation in this study was achieved using a Nd-YAG laser with a 532 nm, 5 ns full-width-half-maximum (FWHM) pulse at 10 Hz repetition rate. Data acquisition is triggered by the response of a fast photodiode to the pulse picked off near the sample. The microwave phase shifter on the local oscillator signal path shifts the detection phase to recover the real and imaginary (in-phase/out-of-phase) components of the complex conductivity [38].

Three sets of photoactive semiconducting films are investigated in this study. They include (1) poly(3-hexylthiophene) (P3HT) and [6,6]-phenyl-C61-butyric acid methyl ester (PCBM) blend films, (2) 2,8-difluoro-5,11-bis(triethylsilylethynyl) anthradithiophene (diF TES ADT): PCBM blend film (Fig. S1) (3) methyl ammonium formamidinium lead iodide perovskite, (MA_{0.85}FA_{0.15}PbI₃) film (Fig. S1). The dropcast/spin-coated films were deposited on glass substrates which were secured onto the non-grounded co-planar transmission line by adhesive tape as shown in Fig. 3a. Complex phase calibration measurements utilized a ≈ 1 mm \times 1 mm size piece of copy paper infused with a common ESR spin standard 2,2-diphenyl-1-picrylhydrazyl (DPPH) co-located on the transmission line also secured with adhesive tape (Fig. 3a). All measurements were performed in ambient conditions at room temperature.

2. Results and discussions

Blends of P3HT: PCBM are one of the most studied binary polymer: fullerene systems for organic electronics [14,16,19,20,39–45]. It serves as the model photoactive material to showcase this new technique. The rate of exciton dissociation in P3HT: PCBM blends occurs on an ultrafast time scale (\sim tens to hundreds of femtoseconds) [40]. Here we are interested in the somewhat longer (hundreds of nanoseconds or longer) charge recombination process which ultimately determines overall device performance, and for which TRMC is an ideal tool [46].

During a TRMC experiment, the sample is optically excited by a nanosecond laser pulse and the transient change in bulk conductivity is captured as a function of time. This photoconductivity modulation is detected as a transmission line impedance change. To remove any spurious signals, the experimental output of the interferometer ($\Delta V(t)$) is taken as the difference between the illuminated and non-illuminated measurements. The duration and nature of the subsequent decay enables one to probe the dynamics of carrier recombination. Thus:

$$\Delta V(t) \propto \Delta \sigma(t) \quad (1)$$

The gigahertz complex photoconductivity ($\Delta \sigma$) contains the $\Delta \sigma'$ and $\Delta \sigma''$ conductivity parts of the complex photoconductivity. $\Delta \sigma'$ corresponds to the change in the dielectric loss ϵ'' , while $\Delta \sigma''$ represents the change in the real part (ϵ') of the dielectric constant ϵ [47].

A common method to estimate the magnitude of the transient conductivity perturbation is to extrapolate the value back to the time immediately after the laser pulse (t_p) using an empirical fit (1). Both TPC and TRMC data were fitted using this method. The transient obtained for P3HT: PCBM blend film (1:1 in vol % fraction) (Fig. 1c) was fit to a biexponential function given by the following equation:

$$V(t) = y_0 + A_1 \exp\left(-\frac{t}{\tau_1}\right) + A_2 \exp\left(-\frac{t}{\tau_2}\right) \quad (2)$$

where y_0 is experimental offset, A_1 and A_2 are the amplitudes of each component, t is time, τ_1 and τ_2 are the relaxation times. The two relaxation times observed in these films (10^{-6} s and 10^{-7} s) are distinct and differ by an order of magnitude. They are attributed to the processes involving trapping and de-trapping of holes within the bulk heterojunction (BHJ), and the recombination of mobile holes with trapped electrons in P3HT [39]. The observed change in polarity of the obtained transient at longer relaxation times is assigned to the residual trapped electrons in P3HT: PCBM film. These observations are consistent with previous studies of similar films done using conventional TRMC [39].

2.1. Analysis of TRMC data using a volume limited sample

The recorded signals as functions of some arbitrary $V(t)$ are indeed useful for intra-sample comparisons but lack any sort of reference to universal material properties. In conventional (cavity-based) TRMC, the determination of a so called cavity calibration factor is necessary to relate the observed change in reflected power to changes in overall sample conductivity. Here, we utilize the correlation between a secondary measure of transient photocurrent (TPC) in companion films to create this same calibration.

The TPC experimental arrangement (Fig. 4a) utilized an array of thermally evaporated gold contacts to collect the transient photocurrent. A P3HT: PCBM film (1:1 in vol % fraction) was dropcast across the contacts (5 μ m spacing, 500 mm length) (Fig. S2). The TPC was measured with a fast current amplifier while a DC bias voltage was applied to the contacts. Since TPC is a measure of a long-term transport while TRMC measures in grain mobility the DC bias voltage < 10 V was used to make sure that the measured mobility/recombination rate remains bias independent (< 10 MV/m). The same laser illumination as described above provided the transient injection of charge. The geometry of the probed region is defined by the overlap of the material between electrodes and the laser spot size.

Using the measured TPC and known electrode geometry, one can deduce the photoconductivity (σ_{photo}) using the following expression:

$$\sigma_{\text{photo}} = \left(\frac{I_{\text{signal}}}{V_{\text{bias}}} \right) \frac{L}{A} \quad (3)$$

here, I_{signal} is the recorded transient current signal, and V_{bias} is the applied DC bias (7 V). L is the distance between two electrodes (5 μ m) and A is the cross-sectional area between the electrodes. The recorded σ_{photo} (Fig. 4c) has a similar transient nature as the TRMC measurements.

Upon completion of the TPC measurements, this same unique calibration sample can then be used for TRMC measurements (Fig. 4b). The subsequent transient change in microwave impedance ($V(t)$) (Fig. 4d) can then be directly correlated to the $\sigma_{\text{photo}}(t)$ and provide the necessary absolute reference for the TRMC transients. Correlation was performed by using the peak $V(t)$ and $\sigma_{\text{photo}}(t)$ values taken at the end of the laser pulse at $t = t_p$.

Traditionally the TRMC response is further analyzed as a measure of transient mobility:

$$\Delta \sigma_{\text{Photo/TRMC}} = en \sum_i \mu_i \quad (4)$$

Equation (4) assumes that every photon creates a single positive and negative charge carrier [40]. Here, e is the electronic charge, n is the carrier concentration, and μ_i is the overall carrier mobility (sum of electron and hole mobilities). In the case where no charge carrier recombination takes place on the time scale of the response time of the setup ($t = t_p$), the yield φ , is defined as [39]:

$$\varphi = \frac{nl}{I_0 F_A} \quad (5)$$

I_0 is the intensity of the laser in photons/pulse/unit area and F_A is the

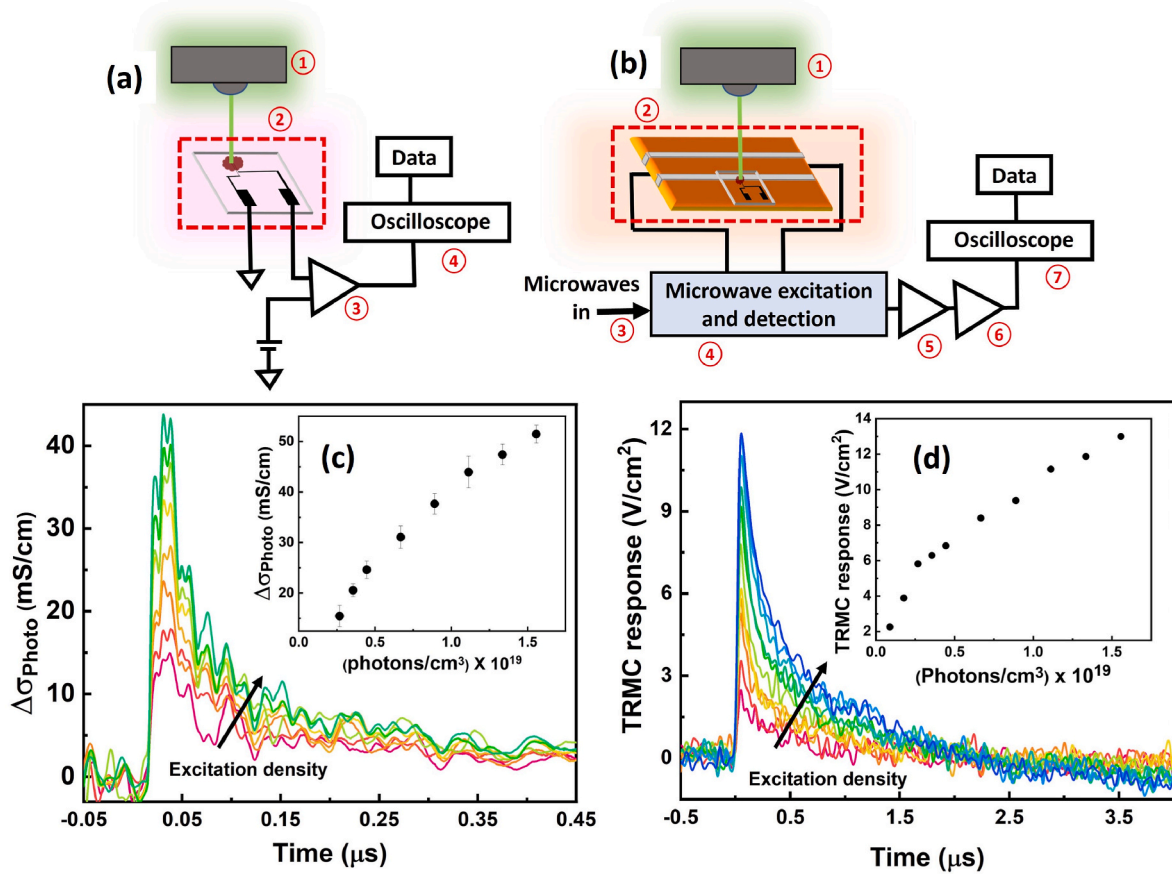


Fig. 4. TPC (a) and TRMC (b) setups for a volume limited sample. TPC (c) and TRMC (d) kinetic traces of a volume limited P3HT: PCBM sample as a function of excitation density under ambient conditions. Insets of (c) and (d) are the excitation density dependence of TPC and TRMC amplitudes. Error bars are defined by signal to noise ratio of the transient. For all the TRMC plots the errors bars are small than the size of the symbol and for TPC errors bars are shown in 4 (c).

optical attenuation (fraction of light absorbed at the excitation wavelength), which is assumed to be one in case of dropcast films. Excitation density ($I_0 F_A / D$) represents the concentration or number density of the excitons produced by the laser pulse, e is the elementary charge and D is the penetration depth of the 532 nm excitation light ($D \sim 100$ nm). The σ_{Photo} and TRMC response at $t = t_p$ as a function of excitation density are shown in the insets of Fig. 4c and d. Using these measured values, a calibration plot shown in Fig. 5a is obtained. The empirical relationship in Fig. 5 holds, provided the microwave interferometer is tuned to the same interference level.

In order to get a uniform sensing region, the sample length along the transmission line is limited to $l < \frac{1}{4} \lambda_{\text{microwaves}}$ (lumped element regime) and the sample is uniformly illuminated by the laser, see Fig. 5b. The change in conductance (ΔG) is given by:

$$\Delta G = \Delta \sigma_{\text{TRMC}} \frac{A}{d} \quad (6)$$

Where, $A = 2g \times l$ is the area, g is the gap of the transmission line, l and d here are length and thickness of the film. These dimensions for a dropcast film on glass secured on a transmission line are shown in Fig. 5b. Finite element simulations (Fig. 3d) show that sample at $g = 150 \mu\text{m}$ lies within the maximum strength of E_1 . With knowledge of the initial excitation density and σ_{TRMC} at $t = t_p$, it is possible to make a first estimation of the mobility. Here, we assume that minimal charge carrier recombination occurs during the laser excitation pulse. Therefore, the yield mobility product, ($\varphi \sum_i \mu_i$) using equations (4)–(6) is given by:

$$\varphi \sum_i \mu_i = \frac{\Delta \sigma_{\text{TRMC}} l}{e I_0 F_A} \quad (7)$$

Fig. 5c and d shows $\Delta \sigma_{\text{TRMC}}$ and $\varphi \sum_i \mu_i$ versus excitation density for this film. The inset of Fig. 5c shows $\Delta G_{\text{TRMC}(t=t_p)}$ versus excitation density for a dropcast film of 20:1 in vol% P3HT: PCBM on glass recorded at 9 GHz microwave frequency. Over an order of magnitude in excitation density, we observe $\varphi \sum_i \mu_i$ in the range of 0.02 and 0.10 $\text{cm}^2 \text{V}^{-1} \text{s}^{-1}$.

This is in agreement with measurements done on similar films and on the transistor device analogs [39,45,46]. As expected, the $\varphi \sum_i \mu_i$ estimated here significantly depends upon excitation density, monotonically reducing with increase in excitation density.

This newly calibrated TRMC measurement protocol was used to investigate five dropcast films across a range of P3HT: PCBM ratios, with 100:1, 20:1, 5:1 and 1:1 wt% P3HT: PCBM as shown in Fig. 6a. These measurements were recorded over a range of laser fluences between 0.3 and 250 $\mu\text{J}/\text{cm}^2$, corresponding to excitation density levels from $\sim 10^{16}$ to $\sim 10^{19}$ photons/ cm^3 . The measurement time window (5 ns–3 μs post laser pulse) is sufficient for quantitative analysis of trapping, detrapping, and recombination processes, which provides information on the carrier dynamics due to time-dependent rate coefficients and mobilities [39, 40]. The excitation density dependence was measured for all films (Fig. 6b). The corresponding transient data are shown in (Fig. S3). Pristine P3HT is known to exhibit high production of free carriers coincident with photoexcitation, even without the presence of an electron acceptor [38]. For the pristine polymer (Fig. S3), all transients decay with a similar profile independent of the laser intensity, with each

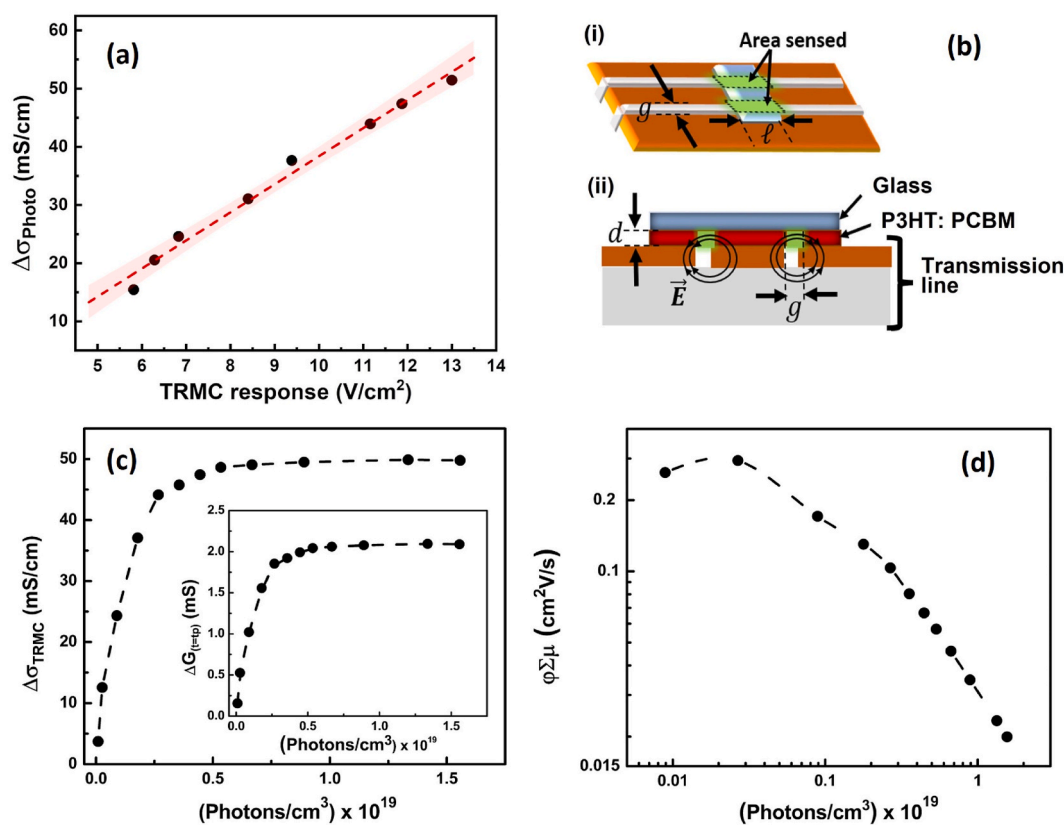


Fig. 5. (a) Calibration plot derived using both TPC ($\Delta\sigma_{\text{Photo}}$) and TRMC response on a volume limited sample (black data points). The red dashed line is the fit to a linear function with 95 % confidence limit. This function is used to estimate the TRMC photoconductivity ($\Delta\sigma_{\text{TRMC}}$). (b) Schematic of the co-planar transmission line (i) and its cross-sectional view (ii) dimensions used in equations (6) and (7). (c) Excitation density dependence of $\Delta\sigma_{\text{TRMC}}$ and $\Delta G_{\text{TRMC}(t=tp)}$ (inset). (d) $\varphi\sum_i\mu_i$, sum of electron and hole mobilities multiplied by the yield determined by TRMC as a function of excitation density for a dropcast film of 20:1 in wt% P3HT: PCBM. (For interpretation of the references to color in this figure legend, the reader is referred to the Web version of this article.)

transient exhibiting a fast decay for the first 50 ns, which then slows at longer times. It should be noted that the use of the highly sensitive detection scheme employed here allows us to measure the pristine polymer at low laser intensities (below 10^{18} photons/cm³) Fig. 6b [39, 40]. At increased levels of laser irradiation, the efficiency of this process is seen to decrease, and the sublinear dependence of the TRMC signal with increasing laser power has been attributed to an exciton-exciton annihilation process that competes with the dissociation process. This is consistent with other cavity-based studies done on similar films [39, 40]. Inclusion of an efficient electron acceptor like PCBM into the polymer allows for competition with this process and thus reduces the efficacy of the annihilation loss mechanism, which is beneficial for organic photovoltaics.

TRMC allows the investigation of charge generation in the donor-acceptor active layer without the need to collect charge at metal contacts. As shown in Fig. 6a the transients corresponding with the four blends show a marked dependence on the PCBM loading. The transients exhibit a long-lived, almost biexponential decay, with the shortest characteristic lifetime for the 100:1 blend and longest for the 1:1 blend (Fig. 6a). Though the transient profiles are like that of the pristine polymer, the signal magnitudes differ substantially. Photoexcitation generates carriers in pairs, but the hole mobility in P3HT is higher than the electron mobility, therefore the dominant contribution to the photoconductance is from the hole term in the P3HT sample. The addition of PCBM and exciton dissociation at the donor-acceptor interface enhances free carrier production (holes in P3HT and electrons in PCBM). Therefore, the recorded signal for the blends is higher compared to that of the pristine P3HT [38,39]. The decay profiles of the blends show distinct dependence on excitation density (Fig. 6b). At high excitation densities,

the light intensity dependence of the hole density becomes sublinear, indicating the presence of a higher-order mechanism that limits free carrier generation. The observed dependence of $\varphi\sum\mu$ on the PCBM loading at low absorbed photon densities extracted using equation (8) is shown in Fig. 6c. The dramatic increase in $\varphi\sum\mu$ for the 100:1 blend versus the neat polymer, followed by only a moderate increase as the wt % of PCBM is further raised to 1:1 is consistent with previous studies [39,40].

Similar measurements were done on a series of thin films with increasing thickness of the 50: 50 P3HT: PCBM blend spincoated onto glass substrates (Fig. S4). A thick layer ensures more photo-absorption, which leads to an increased number of photogenerated carriers. The recorded signal is observed to increase with the increase in the thickness of the film. The decay profiles of the films show distinct dependence on light intensity. Shown in (Figs. S4 and S5) is the film thickness dependence of the peak value of each measured transient. As seen in thinner films at high excitation densities, the hole density becomes sublinear indicating limited free carrier generation.

In the case of contacts-based characterization techniques only carriers generated near the electrodes will be collected and give rise to a photocurrent [11–20]. Because of the low mobility-lifetime products the optimum absorber thicknesses that can be measured using contact-based techniques are often limited to ~ 100 nm or less. Larger absorber thicknesses lead to increased collection losses of charge carriers due to nongeminate recombination that overcompensates the gain in absorbance for most cases. Furthermore, the imbalance of hole/electron mobility values may result in charge accumulation, which shields the electric field and therefore hinders the charge carrier transport and collection. TRMC has the advantage that investigation of charge

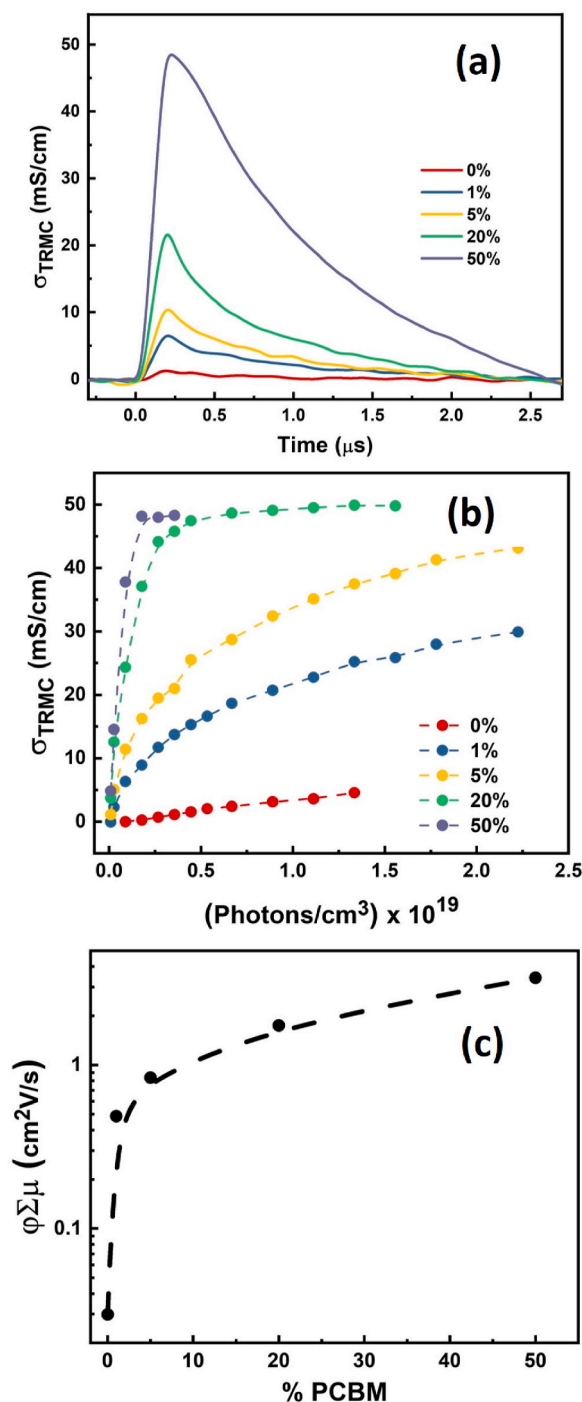


Fig. 6. TRMC kinetic traces of dropcast P3HT:PCBM films at 9 GHz and 10^{17} photons/cm³ excitation density (a). Excitation density dependence (b), and mobility (c) as a function of PCBM concentration.

generation in the donor-acceptor active layer is permitted without needing to collect charge at metal contacts, therefore allowing for an intrinsic investigation of charge generation.

2.2. Microwave phase and frequency

The Mach-Zehnder type microwave interferometer used in this setup is broadband and phase-sensitive [33]. This tuned interferometer has a narrow bandwidth, but it can be readily tuned across a wide range of frequency. Contrary to the narrow band high-Q resonator setup, the convenience of selecting any frequency by tuning the interferometer and

the non-resonant probe makes the overall system broadband.

As recently discussed [38], the microwave detection circuitry allows for direct and calibrated control of the phase of the measured impedance (Figs. S6–9). Since the complex photoconductivity has contributions from both real ($\Delta\sigma'$) and imaginary ($\Delta\sigma''$) components [47], it can be expressed by the following:

$$\Delta\sigma \propto (\Delta\sigma' + i\Delta\sigma'') \quad (8)$$

Earlier efforts to deconvolve the individual complex components of the TRMC response relied on frequency-dependent measurements across the narrow bandwidth of the resonator. No such restrictions exist in this approach and a direct deconvolution can be performed at any arbitrary frequency (within the limitations of the microwave components).

Modulating the experimental detection phase, as in Fig. 7a impacts the measurement of both amplitude and phase transients. Therefore, change in frequency requires the optimization of the phase. Shown in Fig. 7b is an example of a measurement performed by keeping the microwave phase fixed and changing the microwave frequency as a function of excitation density. It should be noted this small change in frequency should have a negligible effect on the recorded signal contrary to what is observed in Fig. 7b. This emphasizes the necessity of the phase optimization.

One of the advantages of having a phase sensitive detection scheme is that it can be used to resolve the complex photoconductivity. The components of the complex photoconductivity, $\Delta\sigma'$ and $\Delta\sigma''$ can be experimentally separated by tuning the microwave phase. It is observed that irrespective of the microwave frequency the transient with $\Delta\sigma'$ is recorded at $n\pi$ and the pure $\Delta\sigma''$ is recorded at $(n+1)\pi/2$ microwave periods (indicated by green circles) in Fig. 7c. For microwave phase calibration the TRMC setup can be readily converted to a continuous wave ESR measurement setup to perform in-situ ESR measurements. An electromagnet capable of supporting X-band ESR measurements (≈ 300 mT) with magnetic field modulation coils shown in Fig. (2) are used to collect the ESR response of the standard DPPH sample. The measured ESR line shape (absorption or dispersion) serves as an unambiguous indicator of the absolute value of the microwave phases at the mixer. This allows one to ‘select’ the corresponding $\Delta\sigma'$ and $\Delta\sigma''$ components of TRMC response (just by changing the microwave phase shifter). Representative transients for both $\Delta\sigma'$ and $\Delta\sigma''$ at different microwave frequencies are shown in Fig. 7d–f. Though the amplitude of the recorded transients is strongly dependent on the detection phase, the overall response is largely frequency independent. The transients were fit to the biexponential functions with the fit parameters and half-life times of the slow components being summarized in Table 1. The ratio of the half-life times “ τ_1/τ_2 ” of the out-of-phase and in-phase transients (Fig. 7d–f) were 0.9–1.2. It is expected from P3HT:PCBM to have a similar in-phase and out-of-phase response and is in agreement with our previous observations [38].

In contrast to the conventional resonator based TRMC measurements, the sensing volume here is defined by the penetration depth of the electric field in the sample (E_1). The magnitude of E_1 is directly proportional to the amplitude of the input microwave signal. Therefore, E_1 can be increased by increasing the amplitude of the input microwave signal and probing deeper into the film. The practical power limit is imposed by the high-frequency excitation and detection circuitry, not the transmission line probe. The input microwave power can be adjusted using the variable attenuator before the splitter (Supporting Fig. S11). The change in attenuation also comes with a concomitant change in microwave phase. Therefore, it is necessary to recalibrate the phase relationship between $\Delta\sigma'$ and $\Delta\sigma''$ each time E_1 is changed. The power dependence for different microwave phases is shown in Supporting Fig. S11. In this normalized plot the signal for the higher power is saturated at the $\pi/2$ phase. The transients corresponding to the highest amplitudes for microwave powers are shown in Supporting Fig. S11. It shows the response of the transients as a function of the input RF power.

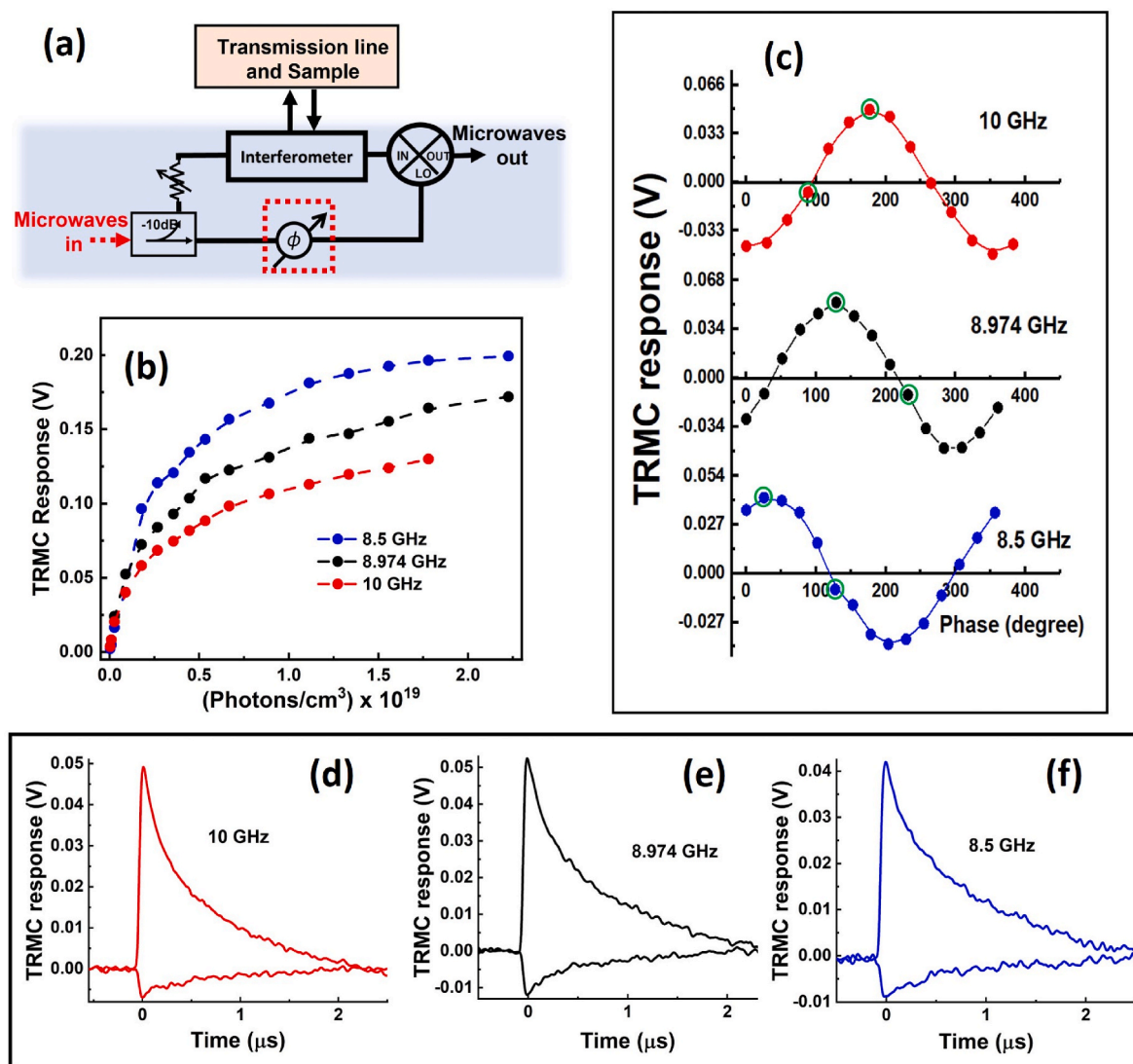


Fig. 7. (a) TRMC schematic for microwave phase and frequencies dependent measurements (variables shown in red), (b) excitation density dependence of TRMC transient amplitude, (c) microwave phase dependence of TRMC transient amplitude and (d–f), TRMC transients of in phase and out of phase components at 9×10^{17} photons/cm³ excitation density for different microwave frequencies. (For interpretation of the references to color in this figure legend, the reader is referred to the Web version of this article.)

Table 1

The fit parameters obtained upon fitting in phase and out of phase (green circles in Fig. 7c) transients recorded at different microwave frequencies/phases (Fig. 7 (d–f)) with a biexponential function.

f (GHz)	A_1	τ_1 (μ s)	A_2	τ_2 (μ s)	$\tau_{1/2}$
8.5	0.32	0.19	0.05	1.68	1.17
	0.04	0.26	0.01	2.10	1.45
8.974	0.47	0.19	0.05	1.58	1.09
	0.05	0.15	0.01	1.41	0.98
10	0.74	0.16	0.05	1.33	.092
	0.04	0.16	0.01	1.27	.098

The decay behavior changes at high RF power and an undershoot behavior appears in the response that was not seen at lower RF power levels. This has been attributed to the linearity of the mixer. The exact details in this process are complex and experimentally put upper limit on the power levels entering the mixer.

The phase sensitive TRMC approach presented here can be used to evaluate photoinduced changes in the relative permittivity [$\Delta\epsilon_r(t) \propto \Delta\sigma(t)$], particularly in ionic semiconductors like MA_{0.85}FA_{0.15}PbI₃ which

are known to exhibit a large relative permittivity ($\epsilon_r \sim 5-50$) [48]. Giant dielectric constant modulation has been reported in metal halide perovskites, where ϵ_r increases by 3 orders of magnitude under illumination from 1 sun conditions at kHz to MHz frequencies [49]. Therefore, this material shows distinct in-phase and out-of-phase TRMC transients at these frequencies (Supporting Fig. S1) [38,50]. In this system, the optical dielectric response due to dielectric permittivity is known to occur over tens to hundreds of picoseconds [48]. TRMC, with nano-second time resolution, is an ideal tool to probe the slower orientational components [48] due to the realignment of dipolar species and the space charge contribution that results from free charges (both ionic and electronic) redistributing over macroscopic distances in the material.

Another possible material to explore using this TRMC technique are diF TES ADT:PCBM blends. Unlike most inorganic counterparts, organic materials exhibit strong exciton binding energies and comparably long spin relaxation times. When investigated as an emitter material in an organic light emitting diode (OLED) type device configuration, diF TES ADT exhibits highly structured positive magneto electroluminescence (MEL) response at room temperature for magnetic fields of \sim mT. [51] This room temperature observable spin-transport phenomenon was attributed to triplet fusion in these materials. In another recent study

[52] diF TES ADT based single crystal transistors were investigated for magnetic field response of the photocurrent. The spin character of the triplets formed by singlet fission was observed. This was highly influenced by the zero-field splitting caused by the magnetic dipole-dipole interaction within the triplet exciton for magnetic fields 0 mT–200 mT. (52) Earlier, cavity based, TRMC studies of pentacene assigned the observed values of $\Delta\sigma'$ and $\Delta\sigma''$ to the migration (oscillation) of charge carriers induced by the alternating electric field of the microwaves. [53] If charge carriers on pentacene move only within a pentacene molecule, the intramolecular migration of the charge carriers contributes primarily to $\Delta\sigma''$ [54] while migration of the charge into adjacent molecules contributes to the $\Delta\sigma'$. The observed phase dependence of the diF TES ADT films (Supporting Fig. S1) extends the utility of the tool to investigate new materials and deduce the photoinduced spin-based transport phenomena in presence of magnetic field.

3. Conclusions

In conclusion, we have demonstrated a novel time resolved microwave conductivity technique, and its calibration for investigating the complex microwave conductivity. This approach utilizes a non-resonant coplanar transmission line and a microwave interferometric detection scheme, which offers several advantages over the traditional cavity based TRMC methods: (1) The measurement sensitivity is no longer dependent on cavity loading but instead determined by tuning of a broadband interferometer. (2) The detection scheme not only enables the measurement of subtle changes in sample photoconductivity upon optical excitation but also allows for investigations of extremely small sample sizes. This capability empowers us to explore device-sized volumes/thicknesses of semiconducting films (nL/nm). (3) The reduction in the probed volume facilitates more direct comparisons with working devices, as opposed to stacked films used in the conventional microwave cavity technique, where film-to-film variation may influence the results. (4) The adoption of a phase-sensitive microwave bridge allows the concurrent use of ESR and TPC measurements as complementary calibration tools to observe absolute changes in photoconductivity. (5) By concurrent ESR measurements of nearby spin standard samples, one can measure phase dependent photoconductivity and deduce the constituent $\Delta\sigma'$ and $\Delta\sigma''$ components without the need for complicated frequency dispersion analysis.

While this demonstration focuses on a series of thin films of P3HT:PCBM on glass, it is important to note that our technique is not limited to polymer blends. The applicability of this approach has also been demonstrated on a series of diF TES ADT and MA_{0.85}FA_{0.15}PbI₃ films spin cast on glass substrates (supporting information Fig. 1). Hence, this versatile technique can be extended to routine studies of other volume limited semiconductors.

4. Materials and methods

P3HT:PCBM thin films of Poly(3-hexylthiophene) (P3HT, >98 % head-to-tail regioregularity) and [6,6]-phenylC61-butyric acid methyl ester (PCBM). Solutions of 20 mg/mL total solid content, with 1:1 wt ratio P3HT:PCBM, were prepared in chlorobenzene. Films were prepared by spin-coating at 1000 rpm onto glass substrates, or by drop casting, followed by an annealing step, 5min at 150 °C, inside a nitrogen filled glovebox (<0.1 ppm O₂, <0.1 ppm H₂O).

CRedit authorship contribution statement

Jaaleen K. Bindra: Conceptualization, Data curation, Formal analysis, Investigation, Methodology, Project administration, Validation, Writing – original draft, Writing – review & editing. **Pragya R. Shrestha:** Investigation, Methodology, Validation, Writing – original draft. **Sebastian Engmann:** Investigation, Methodology, Writing – review & editing. **Chad D. Cruz:** Investigation, Methodology, Writing – review &

editing. **David J. Gundlach:** Funding acquisition, Resources, Supervision, Writing – review & editing. **Emily G. Bittle:** Methodology, Supervision, Writing – review & editing. **Jason P. Campbell:** Conceptualization, Data curation, Funding acquisition, Methodology, Project administration, Resources, Supervision, Validation, Writing – original draft, Writing – review & editing.

Declaration of competing interest

The authors declare that they have no known competing financial interests or personal relationships that could have appeared to influence the work reported in this paper.

Data availability

Data will be made available on request.

Acknowledgments

JKB acknowledges the partial support under the Cooperative Research Agreement between the University of Maryland and the National Institute of Standards and Technology Physical Measurement Laboratory, Award 70NANB14H209, through the University of Maryland. SE acknowledges support from the U.S. Department of Commerce, National Institute of Standards and Technology under the financial assistance award 70NANB22H088. Authors thank Dr. Andrei Kolmakov for his help with devices. Valuable guidance and discussions were provided by Dr. N. Abhyankar and Dr. K.P. Cheung at the National Institute of Standards and Technology.

Appendix A. Supplementary data

Supplementary data to this article can be found online at <https://doi.org/10.1016/j.mtadv.2024.100471>.

References

- [1] J. Lim, et al., Nat. Commun. 13 (1) (2022) 4201–4206, <https://doi.org/10.1038/s41467-022-31569-w>.
- [2] Q. Jiang, et al., Science 378 (6626) (2022) 1295–1300, <https://doi.org/10.1126/science.adf0194>.
- [3] V.S. Nair, et al., Sci. Adv. 2 (9) (2016) e1600142, <https://doi.org/10.1126/sciadv.1600142>.
- [4] R.J. Hoofman, et al., Nature 392 (6671) (1998) 54–56, <https://doi.org/10.1038/32118>.
- [5] J. Xu, Science 367 (6482) (2020) 1097–1104, <https://doi.org/10.1126/science.aaz5074>.
- [6] Y. Yamamoto, et al., Science 314 (5806) (2006) 1761–1764, <https://doi.org/10.1126/science.1134441>.
- [7] J.M. Warman, in: Y. Tebata (Ed.), Pulse Radiolysis Time Resolved Conductivity DC to Microwave, CRC Press, Boca Raton, FL, 1991, pp. 101–133.
- [8] S.E. Braslavsky, Pure Appl. Chem. 79 (2007) 293–465, <https://doi.org/10.1351/pac200779030293>.
- [9] S.T. Martin, H. Herrmann, M.R. Hoffmann, J. Chem. Soc., Faraday Trans. 90 (1994) 3323–3330, <https://doi.org/10.1039/FT9949003323>.
- [10] M.P. DeHaas, J.M. Warman, Chem. Phys. 73 (1982) 35–53, [https://doi.org/10.1016/0301-0104\(82\)85148-3](https://doi.org/10.1016/0301-0104(82)85148-3).
- [11] N.T. Binh, L.Q. Minh, H. Bässler, Synth. Met. 58 (1993) 39–50, [https://doi.org/10.1016/0379-6779\(93\)91116-J](https://doi.org/10.1016/0379-6779(93)91116-J).
- [12] S.T. Hoffmann, et al., J. Am. Chem. Soc. 135 (2013) 1772–1782, <https://doi.org/10.1021/ja308820j>.
- [13] A.J. Mozer, et al., Phys. Rev. B 72 (2005) 035217, <https://doi.org/10.1103/PhysRevB.72.035217>.
- [14] M.J. Tan, et al., ACS Appl. Mater. Interfaces 2 (2010) 1414–1420, <https://doi.org/10.1021/am100078g>.
- [15] M. Shkunov, et al., Adv. Mater. 17 (2005) 2608–2612, <https://doi.org/10.1002/adma.200500890>.
- [16] C. Deibel, et al., Synth. Met. 159 (2009) 2345–2347, <https://doi.org/10.1063/1.3005593>.
- [17] A. Baumann, et al., Adv. Funct. Mater. 21 (2011) 1687–1692, <https://doi.org/10.1002/adfm.201002358>.
- [18] S. Chen, et al., Adv. Energy Mater. 1 (2011) 963–969, <https://doi.org/10.1002/aenm.201100300>.
- [19] P.W. Blom, et al., Adv. Mater. 19 (2007) 1551–1566, <https://doi.org/10.1002/adma.200601093>.

- [20] A. Pivrikas, et al., *Prog. Photovolt.* 15 (2007) 677–696, <https://doi.org/10.1002/pip.791>.
- [21] A. Saeki, et al., *Adv. Mater.* 20 (2008) 920–923, <https://doi.org/10.1002/adma.200702463>.
- [22] A. Crovetto, et al., *Chem. Mater.* 31 (2019) 3359–3369, <https://doi.org/10.1021/acs.chemmater.9b00478>.
- [23] J.M. Warman, et al., *Nature* 310 (1984) 306–308, <https://doi.org/10.1038/310306a0>.
- [24] M.P. de Haas, et al., *Adv. Funct. Mater.* 16 (2006) 2274–2280, <https://doi.org/10.1002/adfm.200500882>.
- [25] J.G. Labram, et al., *J. Mater. Chem. C* 5 (2017) 5930–5938, <https://doi.org/10.1039/C7TC01161J>.
- [26] D.B. Straus, et al., *J. Phys. Chem. Lett.* 6 (2015) 4605–4609, <https://doi.org/10.1021/acs.jpcclett.5b02251>.
- [27] T.J. Savenije, et al., *J. Appl. Phys.* 101 (2007) 113718, <https://doi.org/10.1063/1.2745386>.
- [28] F.F. Abdi, et al., *J. Phys. Chem. Lett.* 4 (2013) 2752–2757, <https://doi.org/10.1021/jz4013257>.
- [29] R. Ihly, et al., *Nat. Chem.* 8 (2016) 603–609, <https://doi.org/10.1038/nchem.2496>.
- [30] H. Oga, et al., *J. Am. Chem. Soc.* 136 (39) (2014), <https://doi.org/10.1021/ja506936f>, 13818–1382.
- [31] M.H. Zarifi, et al., *J. Phys. Chem. C* 119 (2015), <https://doi.org/10.1021/acs.jpcc.5b01066>, 14358–14365.
- [32] J.A. Guse, et al., *JoVE* 121 (2017) 55232, <https://doi.org/10.3791/55232>.
- [33] O.G. Reid, et al., *J. Phys. D Appl. Phys.* 50 (49) (2017) 493002, <https://doi.org/10.1088/1361-6463/aa9559>.
- [34] S. Engmann, et al., *ACS Appl. Electron. Mater.* 5 (8) (2023) 4595, <https://doi.org/10.1021/acsaem.3c00745>.
- [35] P.R. Shrestha, et al., *Anal. Chem.* 91 (2019) 11108–11115, <https://doi.org/10.1021/acs.analchem.9b01730>.
- [36] J.P. Campbell, et al., *Anal. Chem.* 87 (9) (2015) 4910–4916, <https://doi.org/10.1021/acs.analchem.5b00487>.
- [37] C.P. Poole, *Electron Spin Resonance: a Comprehensive Treatise on Experimental Techniques*, 1996.
- [38] J.K. Bindra, et al., *J. Phys. Chem. C* 127 (8) (2023) 4203–4209, <https://doi.org/10.1021/acs.jpcc.2c08700>.
- [39] A.J. Ferguson, et al., *J. Phys. Chem. C* 115 (2011) 23134–23148, <https://doi.org/10.1021/jp208014v>.
- [40] T.J. Savenije, et al., *J. Phys. Chem. C* 17 (46) (2013) 24085–24103, <https://doi.org/10.1021/jp406706u>.
- [41] W.J. Grzegorzczak, et al., *J. Phys. Chem. C* 114 (11) (2010) 5182–5186, <https://doi.org/10.1021/jp9119364>.
- [42] T. Moehl, et al., *ChemSusChem* 2 (4) (2009) 314–320, <https://doi.org/10.1002/cssc.200900002>.
- [43] A. Saeki, et al., *J. Am. Chem. Soc.* 134 (46) (2012) 19035–19042, <https://doi.org/10.1021/ja309524f>.
- [44] A. Saeki, M. Tsuji, S. Seki, *Adv. Energy Mater.* 1 (4) (2011) 661–669, <https://doi.org/10.1002/aenm.201100143>.
- [45] T.J. Savenije, et al., *Adv. Funct. Mater.* 15 (8) (2005) 1260–1266, <https://doi.org/10.1002/adfm.200400559>.
- [46] C.C. Lindsay, et al., *Adv. Energy Mater.* 4 (15) (2014) 1400356, <https://doi.org/10.1002/aenm.201400356>.
- [47] E. Lippert, J.D. Macomber (Eds.), *Dynamics during Spectroscopic Transitions: Basic Concepts*, Springer Science & Business Media, 2012.
- [48] J.N. Wilson, et al., *Apl. Mat.* 7 (2019) 010901–010914, <https://doi.org/10.1063/1.5079633>.
- [49] M.J. Hong, et al., *J. Am. Chem. Soc.* 142 (2020) 19799–19803, <https://doi.org/10.1021/jacs.0c07307>.
- [50] E.J. Juarez-Perez, et al., *J. Phys. Chem. Lett.* 5 (2014) 2390–2394, <https://doi.org/10.1021/jz5011169>.
- [51] S. Engmann, et al., *J. Math. Chem. C* 9 (31) (2021) 10052–10064, <https://doi.org/10.1039/D1TC00314C>.
- [52] E.G. Bittle, et al., *J. Math. Chem. C* 9 (35) (2021) 11809–11814, <https://doi.org/10.1039/D1TC01539G>.
- [53] A. Saeki, S. Seki, S. Tagawa, *J. Appl. Phys.* 100 (2) (2006) 023703, <https://doi.org/10.1063/1.2214638>.
- [54] J.M. Schins, *Rev. Sci. Instrum.* 76 (8) (2005) 084703, <https://doi.org/10.1063/1.2008978>.